

Efficient sparse reconstruction algorithm for bioluminescence tomography based on duality and variable splitting

Wei Guo,¹ Kebin Jia,^{1,*} Dong Han,² Qian Zhang,³ Xueyan Liu,⁴ Jinchao Feng,¹
Chenghu Qin,⁵ Xibo Ma,⁵ and Jie Tian^{5,6}

¹College of Electronic Information & Control Engineering, Beijing University of Technology, Beijing 100124, China

²Key Laboratory of Medical Image Computing of Ministry of Education, Northeastern University, Shenyang, Liaoning 11004, China

³Xidian University, School of Life Sciences and Technology, Xi'an, Shaanxi 710071, China

⁴Sino-Dutch Biomedical and Information Engineering School of Northeastern University, Shenyang, Liaoning 110004, China

⁵Intelligent Medical Research Center, Institute of Automation, Chinese Academy of Sciences, Beijing 100190, China

⁶e-mail: tian@ieee.org

*Corresponding author: kebinj@bjut.edu.cn

Received 11 January 2012; revised 2 July 2012; accepted 17 July 2012;
posted 17 July 2012 (Doc. ID 161296); published 7 August 2012

Bioluminescence tomography (BLT) can three-dimensionally and quantitatively resolve the molecular processes in small animals *in vivo*. In this paper, we propose a BLT reconstruction algorithm based on duality and variable splitting. By using duality and variable splitting to obtain a new equivalent constrained optimization problem and updating the primal variable as the Lagrangian multiplier in the dual augmented Lagrangian problem, the proposed method can obtain fast and stable source reconstruction even without the permissible source region and multispectral measurements. Numerical simulations on a mouse atlas and *in vivo* mouse experiments were conducted to validate the effectiveness and potential of the method. © 2012 Optical Society of America

OCIS codes: 170.3010, 170.6960, 170.6280.

1. Introduction

Bioluminescence imaging (BLI) is an emerging molecular imaging modality, which can be used to monitor physiological and pathological activities at the molecular level. This technique is widely adopted for tumor cell detection, drug discovery, and gene expression visualization [1–4]. Bioluminescence tomography (BLT) can three-dimensionally reconstruct the bioluminescent probe in small animals with a

sensitive charge-coupled device (CCD) camera capturing the surface light signals. By combining multiple BLI acquisition with micro-computed-tomography (micro-CT) anatomical structure, BLT can further resolve the depth of source distributions in biological tissues [5].

BLT is a typical ill-posed problem [6]. To compute a meaningful approximate solution, many reconstruction methods for BLT have been developed. Most of those existing methods were adopted to use a multispectral strategy [7–10] and a permissible source region (PSR, also called the region of interest) strategy [10–13] to overcome the ill-posed property of the

problem. Although these strategies improve the reconstruction qualities to a certain degree, they impose some limitations on practical applications. For example, the ill-posedness can be decreased by selecting relatively small domains as the PSR. However, it is not always reliable or feasible to define such a region effectively in practical cases [14]. In addition, spectrally resolved methods can significantly increase signal acquisition time and the computational burden [15].

No matter which strategy is adopted, regularization techniques are usually combined to overcome the ill-posedness and recover source distribution from noisy measurements. Among different regularization methods, the L2-type regularization strategy is the most popular and commonly applied method, which minimizes the output-least-square formulation incorporated with the L2-norm regularization term to stabilize the problem [10–13]. The merit of the regularization with the L2-norm penalty function is that it is simple and easy to solve by standard tools for linear optimization such as the Newton method [12,13,16]. However, it leads to the solution being oversmoothed. This characteristic is not conducive to reconstructing the light source, especially in multiple-source reconstruction cases. In addition, the volumes of the bioluminescent probes are very small compared with the whole reconstruction domain in BLT practical applications. Therefore, several reconstruction algorithms with sparsity regularization have been reported recently [17–20].

Compared with L2-type regularization, the objective function of sparsity regularization is convex but nondifferentiable. Thus, many existing methods with a sparsity regularity strategy are adopted to reformulate them as a convex and differentiable quadratic program with nonnegative constrained conditions and then use efficient iteration methods to optimize them. Lu *et al.* presented a sparsity reconstruction algorithm for spectral BLT based on the diffusion approximation (DA) model where the differentiable approximation method and the limited-memory variable metric bound constrained quasi-Newton method were used to optimize the objective function [17]. He *et al.* developed a sparsity reconstruction method with the multilevel finite element method (FEM) approach for solving the BLT inverse problem and combined an interior-point method with the preconditioned conjugate gradients algorithm (l1_ls) to solve the constrained problem [18]. Gao *et al.* proposed an approach based on the radiative transfer equation (RTE) and multilevel FEM, in which a standard interior-point method was applied to regularize the inverse source recovery [19]. The aforementioned methods demonstrate the feasibility and potential of sparsity regularization with numerical simulation and phantom experiments. However, those reconstruction algorithms require either a PSR or multispectral measurements. Furthermore, when the matrix A [a system matrix in the linear relationship of the BLT inverse problem,

defined in detail in Eq. (5)] is dense, reconstruction algorithms for BLT based on the interior-point methods do not display their optimal performance and require a long computation time [20]. Recently, as the standard algorithm for solving the problem of Lp regularization [21], an iterative shrinkage algorithm (IST) has been successfully applied in fluorescence molecular tomography [22]. However, the iterative-shrinkage-based method belongs to the class of first-order algorithms, and its convergence rate is relatively slow, especially when the regularization parameter is very small or the problem is very ill-posed [23].

In this work, a sparsity regularity algorithm based on duality and variable splitting [24,25] is proposed. We transformed the L1-norm minimization problem into a dual optimization problem by using the duality and variable splitting and handle the resulting constrained problem via an augmented Lagrangian (AL) scheme. In the proposed method, only the dual variable was iteratively computed in a subproblem, and the primal variable of the source distribution was obtained from computing soft thresholding with the final result of the dual variable. Additionally, the sparsity of the primal variable was explicitly used in the subproblem to reduce the computational cost. Therefore, our method can obtain fast, stable source reconstruction even without the permissible source region and multispectral measurements. To show the merits of the method, we compared it with the other two methods. The results of the simulations in the mouse atlas and *in vivo* mouse experiments validated the performance of our method.

This paper is organized as follows. Section 2 presents the photon propagation model, its linear relationship with the FEM, and the proposed algorithm. In Section 3, the numerical simulations in a heterogeneous mouse atlas and *in vivo* mouse experiment are conducted to evaluate the performance of the proposed method. Finally, we discuss the results and conclude this paper.

2. Method

A. Photon Propagation Model

The RTE is considered the most accurate model for describing the process of photon propagation in biological tissues. However, RTE is computationally expensive. Generally, approximations of RTE such as the DA model, simple spherical harmonics, spherical harmonics, and discrete ordinates are more commonly used. Among all the approximate models, the DA is the most popular one [26,27]:

$$-\nabla \cdot D(r) \nabla \Phi(r) + \mu_a(r) \Phi(r) = S(r) \quad (r \in \Omega), \quad (1)$$

where Ω is the whole reconstruction domain, $\Phi(r)$ represents the photo fluence rate, $S(r)$ provides the source energy distribution, $\mu_a(r)$ is the absorption coefficient, $\mu'_s(r)$ is the reduced scattering coefficient, and $D(r) = 1/3(\mu_a(r) + \mu'_s(r))$ indicates the optical diffusion coefficient. Because the bioluminescence

imaging experiment is generally performed in a totally dark environment, no photon travels into Ω through the boundary $\partial\Omega$. Therefore, the DA is subject to the Robin boundary condition,

$$\Phi(r) + 2A(r; n, n')D(r)(v(r) \cdot \nabla \Phi(r)) = 0 \quad (r \in \partial\Omega), \quad (2)$$

where $\partial\Omega$ donates the boundary of the whole reconstruction domain and $A(r, n, n')$ represents the mismatch coefficient between Ω and its surrounding medium. The measured quantity is the outgoing photon density of $\partial\Omega$, which can be expressed as follows [28]:

$$\begin{aligned} Q(r) &= -D(r)(v(r) \cdot \nabla \Phi(r)) \\ &= (2A(r; n, n'))^{-1}\Phi(r), \quad (r \in \partial\Omega). \end{aligned} \quad (3)$$

B. Linear Relationship Establishment

Equations (1) and (2) are converted into the following matrix-form equation. A linear relationship between the source distribution inside the heterogeneous medium and the photon fluence rate on the surface can be established by the finite element techniques:

$$P\Phi = FS, \quad (4)$$

where P is the positive definite matrix, Φ is the measurable photon flux photon on the boundary nodes, F is the source weight matrix, and S is the source distribution on the interior nodes. The nonmeasurable entries in Φ and corresponding rows in $P^{-1}F$ can be removed, which establishes a new linear relationship [29]:

$$AS = \Phi^m, \quad (5)$$

where $A \in R^{M \times N}$ and Φ^m is the boundary measurement.

C. Reconstruction Based on Dual AL

As mentioned, BLT is the typical ill-posed inverse problem. The most popular method for source reconstruction is to formulate it as a least-square optimization problem. In view of the sparsity of the source and the insufficiency of the measurable data, it is natural and sensible to select the L1-norm as the regularization term. Thus Eq. (5) can be converted into the following unconstrained optimization formulation:

$$\min J(w) = \frac{1}{2} \|Aw - \Phi^m\|_2^2 + \lambda \|w\|_1, \quad (6)$$

where λ is the regularization parameter. It is popular to cast the problem in Eq. (6) as a convex one. Therefore, the previous methods tend to approximately

regard the problem as the basis pursuit problem [17–19]:

$$\min \|w\|_1 \text{ subject to } Aw - \Phi^m = 0. \quad (7)$$

Unlike the existing L1-norm regularization reconstruction method for BLT, in this work, we converted Eq. (6) into the following dual problem [30]:

$$\begin{aligned} \max E(\alpha, \nu) &= -\frac{1}{2} \|\alpha - \Phi^m\|^2 + \frac{1}{2} \|\Phi^m\|^2 \\ &\quad - \delta_\lambda^\infty(\nu) \text{ subject to } \nu - A^T \alpha = 0, \end{aligned} \quad (8)$$

where the Fenchel duality theorem was used. δ_λ^∞ is the indicator function. $\delta_\lambda^\infty = 0$ if $\|\delta\|_\infty < \lambda$ and $\delta_\lambda^\infty = \infty$ otherwise. The sizes of α and w are $M \times 1$ and $N \times 1$, respectively. Here, M is the number of nodes on the surface and N is the number of all nodes in the body. As for BLT, the dual problem can play an important role in reducing computational cost. The denser the mesh or the more complex the construction of the tissue, the more computational cost can be saved. The AL function for the dual problem is defined as

$$L(\alpha, \nu, w, \mu) = E(\alpha, \nu) - w^T(A^T \alpha - \nu) - \frac{\mu}{2} \|A^T \alpha - \nu\|_2^2, \quad (9)$$

where w is a vector of the Lagrange multiplier and corresponds to the source distribution on nodes in the primal problem. μ is the barrier parameter [31]. The main steps of the AL method consists in maximizing $L(\alpha, \nu, w, \mu)$ with respect to (α, ν) , keeping w fixed, then updating (α, ν) , and repeating these two steps until stopping criteria are satisfied. Here, the maximizer (α, ν) of Eq. (9) is used to update the Lagrangian multiplier w as follows:

$$w_{k+1} = w_k + \mu_t(A^T \alpha_t - \nu_t). \quad (10)$$

Note that the terms involved in Eq. (9) and Eq. (10) can be decoupled into a set of one-dimensional ones; therefore we further carried out the maximization of the AL function in Eq. (9) with respect to ν in a closed form as follows:

$$\begin{aligned} L(\alpha, \nu, w, \mu) &= -\frac{1}{2} \|\alpha - \Phi^m\|^2 + \frac{1}{2} \|\Phi^m\|^2 \\ &\quad - \sum_{j=1}^N \left(\frac{\mu}{2} \left(\nu_j - \left(\frac{w}{\mu} + A^T \alpha \right)_j \right)^2 + \delta_\lambda^\infty(\nu_j) \right), \end{aligned} \quad (11)$$

where ν_j denotes the j th element of ν . Consequently, the maximizer $\nu(\alpha)$ is given as follows:

$$\nu(\alpha) = \text{CL}_\lambda \left(\frac{w}{\mu} + A^T \alpha \right), \quad (12)$$

where CL_λ is the clipping function. By substituting the above ν back into Eq. (8), we can obtain the maximizer $L(\alpha, w, \mu)$ and the Lagrange multiplier w as follows:

$$\max L(\alpha, w, \mu) = \max -\frac{1}{2} \|\alpha - \Phi^m\|_2^2 - \frac{\mu}{2} \left\| \text{Shrink}_\lambda \left(A^T \alpha + \frac{w}{\mu} \right) \right\|_2^2, \quad (13)$$

$$w_{k+1} = \text{Shrink}_{\lambda\mu_k}(w_k + \mu_k A^T \alpha_k), \quad (14)$$

where k donates the iterative step. $\text{Shrink}_{\lambda\mu_k}$ is the well-known soft threshold function and is defined as follows [23]:

$$\text{Shrink}_\lambda(w) = \left(\max(|w_j| - \lambda, 0) \frac{w_j}{|w_j|} \right)_j \quad (j=1, \dots, n). \quad (15)$$

We next address the solution of the inner iteration, Eq. (13). The inner maximization problem in Eq. (13) is a linear least-squares problem, and several optimization algorithms can be adopted. In this work, the preconditioned conjugate gradient method is employed due to its better performance in large-scale linear inverse problems, which is presented in algorithm 2 [32]. Here, the preconditioner only consists of the diagonal elements of the Hessian matrix:

$$P = \text{diag}(\nabla^2 L(\alpha)) = \text{diag}(-I_m - \mu_k A_+ A_+^T), \quad (16)$$

where A_+ is the submatrix of A that consists of active columns with indexes $J_+ = \{j \in \{1, 2, \dots, n\} : |w_k + \mu_k A^T \alpha| > |\lambda \mu|_k\}$. I_m is the identity matrix of size m . It is noted that Hessian computational complexity is only proportional to the number of active components of $w_k + \mu_k A^T \alpha$. Thus, the sparser the solution α becomes, the faster the computation of a Newton step becomes.

There were two parameters needed for manual initialization besides the regularization parameter and stopping criterion, including the initial value of barrier parameter μ and its increasing rate. The larger initial value and increasing rate could accelerate the convergence rate by saving both the computation required for each outer iteration and inner iteration. However, this also risks making the condition of the problem worse. Therefore, we used the conservative setting for the sequence of μ . The initial value of μ was set to be $0.01/\lambda$, and μ_k was increased by a factor of 2. In fact, by using the above conservative setting, the performance of the proposed method could reach a compromise between efficiency and

Table 1. Optical Parameters of Each Organ in the Mouse Atlas [34]

	Muscle	Heart	Lungs	Liver	Spleen	Bone
μ_a (mm ⁻¹)	0.032	0.022	0.071	0.128	0.075	0.002
μ'_s (mm ⁻¹)	0.586	1.129	2.305	0.646	2.178	0.935

stability. Algorithm 1 summarizes the proposed algorithm.

Algorithm 1. Dual AL Algorithm

```

1: Initialize  $\mu_1, k_{\max}, \text{tol}$ ;
2: while  $\|(J(w)^k - J(w)^{k-1})\| / \|\Phi^m\| \geq \text{tol}$  or  $k \leq k_{\max}$ , do
3: Compute  $ak + 1$  in Eq. (13) using Algorithm 2;
4: Update the primary variable  $wk + 1$  by Eq. (14);
5: Update the barrier parameter  $\mu_{k+1} = 2\mu_k$ ;
6: Update  $k \leftarrow k + 1$ ;
7: End while

```

Algorithm 2. Preconditioned Conjugate Gradient Method

```

1: Input  $\alpha, w, \mu, \Phi^m, A^T, \varepsilon, k = 0$ ;
2: Repeat;
3: Compute the search direction  $\Delta\alpha_k$  as an approximate solution to the Newton system by preconditioned conjugate gradient, where the preconditioner is calculated by Eq. (16);
4: Compute the step size  $\gamma$  by backtracking the line search;
5: Update the iteration by  $\alpha_{k+1} = \alpha_k + \Delta\alpha_k \cdot \gamma$ ;
6: Update  $k \leftarrow k + 1$ ;
7: Until  $\gamma \leq \varepsilon$ 

```

3. Experiments and Results

A. Simulation Verifications

1. Single-source Case

Heterogeneous simulation experiments were conducted to illustrate the performance of the proposed reconstruction method. In order to approximate the real situation as much as possible, the simulation was based on the mouse atlas. The atlas was constructed by our group, and more details can be found in [14,33]. In our simulation experiments, we selected the torso section of the mouse atlas as the region to be investigated, which was 25 mm in height and consisted of six tissues including muscle, lungs, heart, liver, spleen, and bone. The optical properties for tissues are listed in Table 1 [34]. As mentioned for BLT, the volume of the bioluminescent sources is

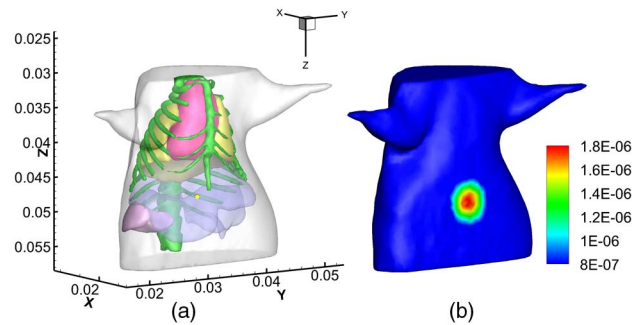


Fig. 1. (Color online) Reconstruction model with a single source. (a) Torso of the mouse atlas model with one source in the liver; (b) Simulated photon distribution on the surface.

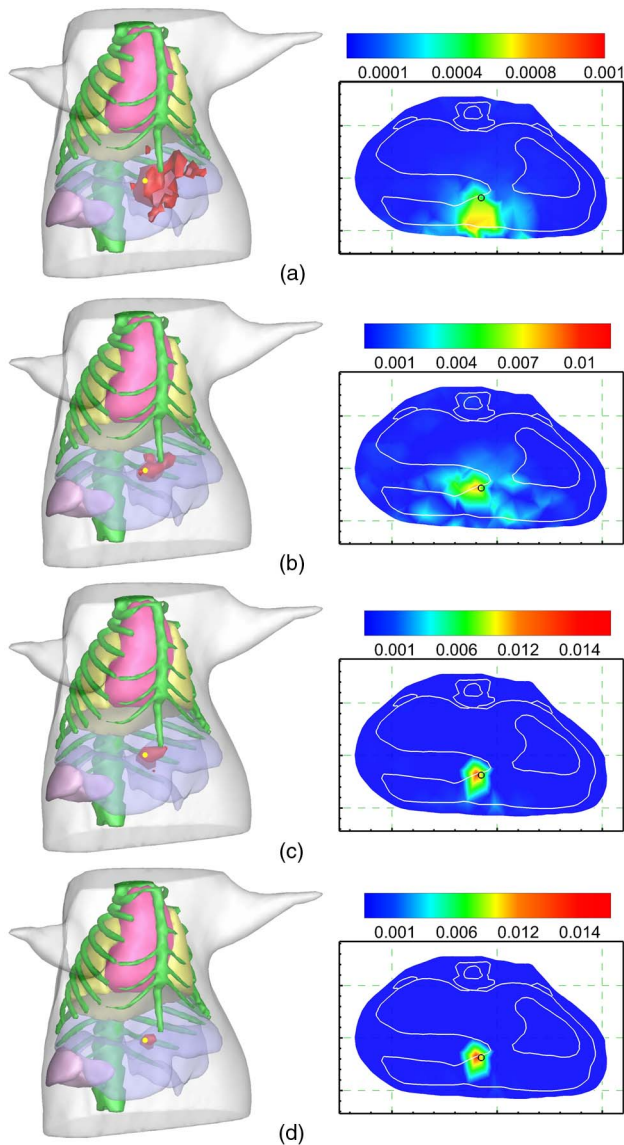


Fig. 2. (Color online) Comparison of the reconstruction results. (a), (b), (c), and (d) are the reconstruction results with Newton-L2 (without PSR), Newton-L2 (with PSR), IS-L1, and the proposed method, respectively. The results are shown in the form of iso-surfaces for 40% of the maximum value (left column) and slice images in the $z = 47.29$ mm plane (right column). The small yellow sphere in the iso-surfaces view image and the circles in the slice images denote the real position of the bioluminescent source.

always small and sparse, that is, as necessary for early detection of tumors. Therefore, small spherical sources were used in the simulation verification.

For the forward problem, FEM was employed to generate the synthetic measurements. The atlas

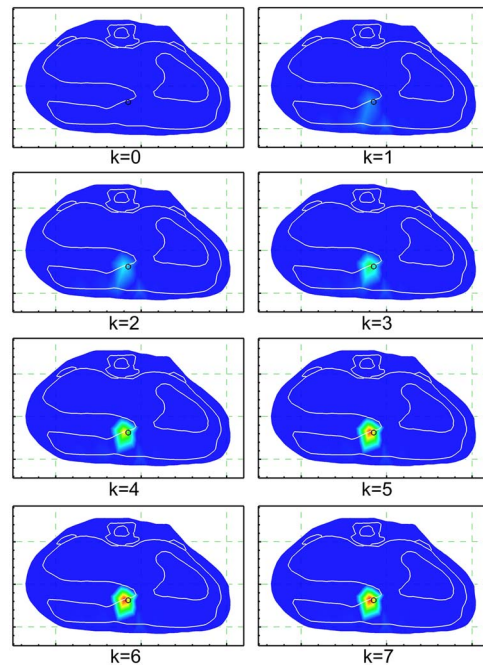


Fig. 3. (Color online) Reconstruction results with k th outer iteration.

model with the interior bioluminescent source was discretized into a tetrahedral-element mesh consisting of 30,998 nodes and 167,841 tetrahedral elements. The bioluminescent sources were 0.6 mm in diameter and were located in the liver, with the center at (18.24, 31.58, 47.29) (the units are in millimeters), as shown in Fig. 1(a). The density of the bioluminescent source is set to be 2.0 nWatts/mm^3 . Figure 1(b) shows the simulated photon distribution on the surface. The reconstruction mesh consisted of 4,093 nodes and 20,068 tetrahedral elements. By removing the points on the top cross section and bottom cross section, there were 1166 measurement nodes and 3624 unknowns. The proposed method could be competent for whole-body bioluminescence tomography. Therefore, the size of the system matrix was 1166×3624 .

The reconstruction results were evaluated quantitatively in terms of reconstruction time, location error, and maximum reconstruction value. We defined the location error to be $LE = |S_{\text{recon}} - S_{\text{real}}|$, where S_{real} is the real location of the source center and S_{recon} is the location of the node with the maximum reconstructed value for that source.

To better illustrate the performance of the proposed method, we compared the proposed method

Table 2. Quantitative Comparisons of Reconstruction Results

Recon. Method	Recon. Position (mm)	LE (mm)	Recon. Time (s)	Maximum Recon. Value (nW/mm ³)
Newton-L2	(14.45, 35.50, 45.75)	5.6684	1301.7	0.00104
Newton-L2 (with PSR)	(18.19, 34.25, 46.40)	2.8132	215.6	0.01042
IS-L1	(18.26, 31.97, 47.28)	0.3995	237.9	0.01363
Proposed method	(18.26, 31.97, 47.28)	0.3995	4.51	0.01434

Table 3. Quantitative Information about Reconstruction Results with k th Outer Iteration

k th	$J(x)$	Maximum Recon. Value (nW/mm ³)	Number of Inner Iteration	Time (s)
0 (Initial value)	0	0	—	—
1	2.58068e-11	0.00200	10	1.2065
2	1.00169e-11	0.00394	3	0.1874
3	9.88048e-13	0.00681	3	0.2365
4	9.77913e-13	0.01072	3	0.3096
5	9.62687e-13	0.01379	6	0.5587
6	9.67595e-13	0.01433	6	0.8528
7	9.62326e-13	0.01434	5	1.1052

Table 4. Quantitative Comparisons of Reconstruction Results with Different Gaussian Noise Levels

Noise Level	Recon. Method	Recon. Location Center (mm)	LE (mm)	Recon. Time (s)	Maximum Recon. Value (nW/mm ³)
5%	Newton-L2	(15.06, 40.46, 53.91)	11.5296	1360.3	0.00676
	Newton-L2(with PSR)	(18.19, 34.25, 46.40)	2.8132	206.6	0.02293
	IS-L1	(18.26, 31.97, 47.28)	0.3995	244.7	0.01162
	Proposed method	(18.26, 31.97, 47.28)	0.3995	4.93	0.01250
10%	Newton-L2	(15.89, 43.03, 53.58)	13.2826	1347.8	0.00797
	Newton-L2(with PSR)	(25.37, 30.38, 49.27)	7.4944	218.6	0.01192
	IS-L1	(18.26, 31.97, 47.28)	0.3995	241.2	0.01016
	Proposed method	(18.26, 31.97, 47.28)	0.3995	5.35	0.01108
15%	Newton-L2	(15.30, 17.26, 33.11)	20.3579	1341.6	0.00892
	Newton-L2(with PSR)	(18.19, 34.25, 46.40)	2.8132	205.6	0.01778
	IS-L1	(18.26, 31.97, 47.28)	0.3995	226.4	0.00868
	Proposed method	(18.26, 31.97, 47.28)	0.3995	4.94	0.01003

with the IST-based method (IS-L1) [22] and Tikhonov regularization method [12,13,16]. Both of them are typical methods for optical reconstruction. The former can be viewed as an extension of the classical

gradient algorithm and is attractive due to its simplicity. Here, we calculated the step size of IST using the method introduced in [22] and set the maximum iteration number to be 100000. In our experiments,

Table 5. Quantitative Information about Reconstruction Results with k th Outer Iteration for Different Levels of Noise

Noise Level	k th	$J(x)$	Maximum Recon. Value (nW/mm ³)	Number of Inner Iteration	Time (s)
5%	0 (Initial value)	0	0	—	—
	1	2.79457e-11	0.00168	12	1.4417
	2	3.39168e-12	0.00307	3	0.1995
	3	3.38357e-12	0.00531	3	0.3303
	4	3.37738e-12	0.00857	4	0.4859
	5	3.37053e-12	0.01133	4	0.6593
	6	3.36685e-12	0.01231	4	0.7179
	7	3.36641e-12	0.01250	5	1.0511
10%	0 (Initial value)	0	0	—	—
	1	2.86798e-11	0.00156	9	1.2666
	2	3.29571e-12	0.00278	3	0.2966
	3	3.29003e-12	0.00458	3	0.3423
	4	3.28576e-12	0.00693	3	0.4162
	5	3.28195e-12	0.00922	3	0.4900
	6	3.27976e-12	0.01055	6	1.0265
	7	3.27923e-12	0.01108	6	1.4625
15%	0 (Initial value)	0	0	—	—
	1	2.83062e-11	0.00142	10	1.2854
	2	3.31427e-12	0.00246	4	0.3002
	3	3.30929e-12	0.00400	3	0.2832
	4	3.30605e-12	0.00598	4	0.4146
	5	3.30334e-12	0.00798	4	0.7073
	6	3.30171e-12	0.00948	5	0.8368
	7	3.30099e-12	0.01003	6	1.0690

we reconstructed the source with the Tikhonov regularization method in two different cases. In first case, there was no PSR employed, which was similar with the conditions of IS-L1 and the proposed method. In the second case, we defined $\{(x, y, z) | 46 \leq z \leq 50\}$ as the PSR, and there were 666 nodes in the reconstruction region. We used a limited-memory variation of the Broyden–Fletcher–Goldfarb–Shanno (LBFGS) method to solve the objective function of Tikhonov regularization, because the Newton method is a second-order optimization method. Here, we set the maximum iteration number for the LBFGS to be 800. The regularization parameter for the three methods was manually optimized. Finding the optimal or near-optimal regularization parameters automatically will be our future work. All of the reconstructions were carried out on a personal computer with Intel Core2 Duo processor, 3.2 GHz, and 2 GB RAM.

The comparison experiment using the three methods was performed. The visual effects of the reconstruction results are presented in the form of slice images and iso-surfaces as shown in Fig. 2. The quantitative information is also listed in Table 2. It can be seen that both IS-L1 and the proposed method could obtain satisfactory source location and maximum reconstruction value. The reconstruction result of Newton-L2 was oversmoothed and highly dependent on the selection of PSR, and its performance was inferior to the other two methods. As for the proposed method, it not only performed slightly better than IS-L1 in terms of maximum reconstruction value, but it was also about 50 times faster than IS-L1.

Due to an improved direction and an automatic step-size selection mechanism, the proposed method could obtain better results within 5 s. In the experiment, the reconstruction was completed when the number of outer iterations (the number of updated primal variables) was 7. In contrast, it was

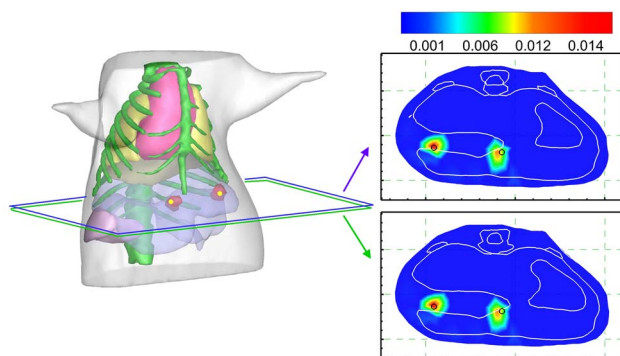


Fig. 4. (Color online) Reconstruction results in the double-source case. The results are shown in the form of iso-surfaces for 40% of the maximum value (left column). Slice images in $z = 47.06$ mm and 47.29 mm planes (right column) were selected to show the results in more detail. The small yellow sphere in the iso-surfaces view image and the circles in the slice images denote the real position of the bioluminescent source.

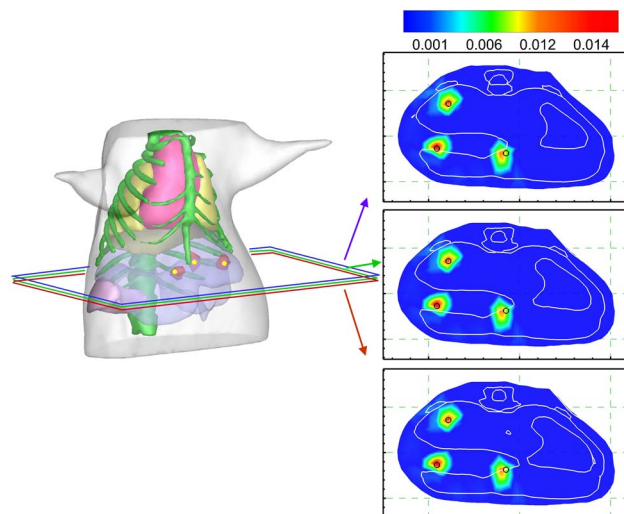


Fig. 5. (Color online) Reconstruction results in the double-sources case. The results are shown in the form of iso-surfaces for 40% of the maximum value (left column). Slice images in $z = 47.06$ mm, 47.29 mm, and 47.45 mm planes (right column) were selected to show the results in more detail. The small yellow sphere in the iso-surfaces view image and the circles in the slice images denote the real position of the bioluminescent source.

100000 for IS-L1. A set of slice images for the reconstruction results corresponding to the k th outer iteration is shown in Fig. 3, and the quantitative data are listed in Table 3, where $J(x)$ is the value of the objective function in Eq. (6).

2. Reconstructions with Different Noise Levels

It is well known that the ill-posed nature of BLT makes the reconstruction sensitive to measurement noise. We performed simulations based on measurements with different levels of Gaussian noise to evaluate the robustness and stability of the proposed method. The heterogeneous model and the setting of source were the same as those in previous subsection. Gaussian noise at 5%, 10%, and 15%, respectively, was added to the synthetic measurements. The quantitative reconstruction results are compiled in Table 4. We found that both IS-L1 and the proposed method could localize the source from the whole body, even in the presence of noise. Compared with IS-L1, the proposed method could produce comparative quantitative results. However, its reconstruction time was about 45 times that of IS-L1.

Table 6. Reconstruction Results in Double-source Case

Source Number	Actual		Location		Maximum Recon. Value (nW/mm ³)
	Position (mm)	Recon. Location Center (mm)	Error (mm)		
1	(18.74, 39.15, 47.06)	(18.75, 39.20, 46.86)	0.2064		0.0163
2	(18.24, 31.58, 47.29)	(18.26, 31.97, 47.28)	0.3995		0.0145

Table 7. Reconstruction Results in Multiple-source Case

Source Number	Actual Position (mm)	Recon. Location Center (mm)	Location Error (mm)	Maximum Recon. Value (nW/mm ³)
1	(18.74, 39.15, 47.06)	(18.75, 39.20, 46.86)	0.2064	0.0167
2	(18.24, 31.58, 47.29)	(18.26, 31.97, 47.28)	0.3995	0.0146
3	(23.60, 37.94, 47.45)	(23.60, 37.97, 47.65)	0.2023	0.0156

Additionally, to describe the process of the reconstructions in more detail, the reconstruction results corresponding to the k th outer iteration for each level of noise are listed in Table 5.

3. Double-source Case and Multiple-source Case

With respect to multisource intensities and depths, a two-source-setting simulation and a three-source-setting simulation were considered in evaluating the proposed method. Both forward mesh and reconstruction mesh have the same size as those used in the single-source case. All of the sources were placed in the liver and had the same size as the one used in the single-source case. Their position centers and intensities were (18.24, 31.58, 47.29) and 2, (23.60, 37.94, 47.45) and 1.8, and (18.74, 39.15, 47.06) and 1, respectively. Figure 4, Fig. 5, Table 6, and Table 7 show the reconstruction results for different source

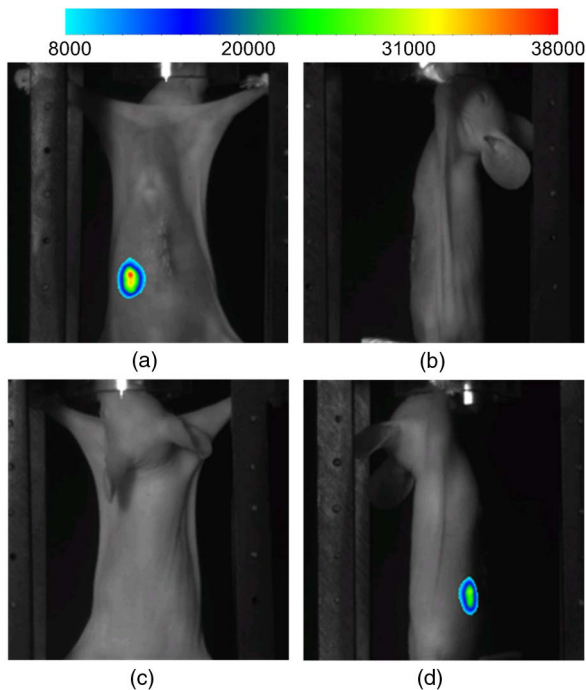


Fig. 6. (Color online) Multiview superimposed images of photographs and luminescent images. (a), (b), (c), and (d) are 0°, 90°, 180°, and 270° views, respectively.

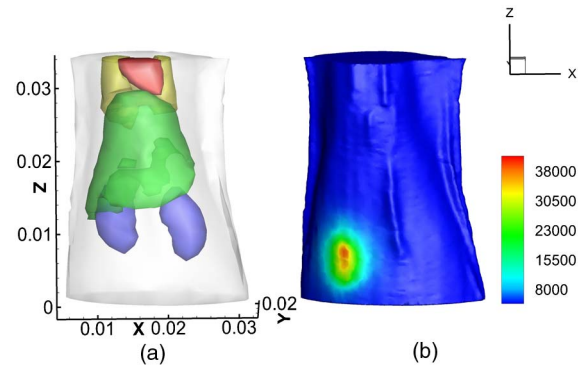


Fig. 7. (Color online) *In vivo* heterogeneous model. (a) Torso of the model. (b) Three-dimensional photon distribution on the surface resulting from two-dimensional bioluminescence photographs.

setups in the form of slice images along with iso-surfaces for 40% of the maximum value and quantitative data. We found that the sources can be distinctly distinguished and accurately reconstructed.

B. In Vivo Experiment

In this subsection, an *in vivo* experiment was performed to further evaluate the proposed algorithm. The experiment was conducted in the dual-modality optical/micro-CT *in vivo* imaging prototype system developed in our lab [35–37]. A nude, hairless mouse (Nu/Nu, Laboratory Animal Center, Peking University, China) was used in this experiment. The test luminescent source implanted into the abdomen of a nude mouse was a transparent catheter filled with luminescent liquid. The source had a similar emission spectrum with the firefly luciferase-based source. It was about 1 mm in diameter and 2.5 mm long.

The optical data, including photographs and luminescent images, were captured by a CCD camera (Princeton Instruments VersArray 1300B, Roper Scientific, Trenton, NJ) from four directions at 90 deg intervals. To reduce dark current noise and increase intensity of luminescent signals, the CCD was cooled to -110°C using liquid nitrogen, and the integration time was set to 120 s. The four-view superimposed images of photographs and luminescent images are shown in Fig. 6. After finishing optical acquisition, the anesthetized mouse was scanned using micro-CT. According to the information based on anatomical structures, the CT image was segmented into the heterogeneous model including muscle, heart, liver, lungs, and kidneys, as shown in Fig. 7(a). The optical parameters for the tissues are listed in Table 8 [34,38]. Then a landmarks-based rigid-body registration method was adopted in this work to register

Table 8. Optical Parameters of Each Organ in the Heterogeneous Model [34,37]

	Muscle	Heart	Lungs	Liver	Kidneys
μ_a (mm ⁻¹)	0.008	0.138	0.456	0.829	0.150
μ'_s (mm ⁻¹)	1.258	1.076	2.265	0.735	2.507

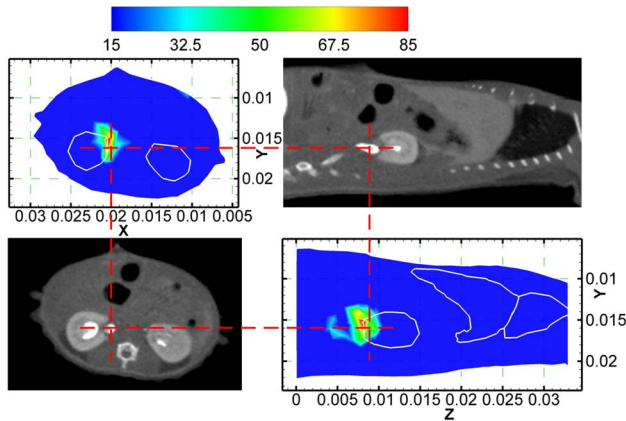


Fig. 8. (Color online) Reconstruction results: transverse view of the results and comparisons with the corresponding CT slices. The cross of the red lines denotes the actual source center.

CT data with the bioluminescent images [36]. After the registration, the absolute irradiance distribution in two-dimensional bioluminescent images was mapped on the three-dimensional mouse surface. The photon distribution onto the surface is shown in Fig. 7(b). Additionally, the bioluminescent source was easily distinguished in CT images, and the actual center of the source was (20.05, 16.18, 8.46).

The torso consisted of 1832 nodes and 9072 tetrahedral elements. The reconstruction took 3.46 s. The reconstruction center position of the source was (20.46, 15.23, 8.11) with a deviation of 1.05 mm to the actual center, and the final reconstructed results of the proposed method are shown in Fig. 8.

4. Conclusion

In this paper, the BLT problem based on L1-norm regularization was transformed into a dual problem, and the resulting constrained problem was attacked with an AL scheme. The proposed method is based on the dual sparse reconstruction problem and explicitly uses the sparsity of the primal variable. Thus the proposed approach is accomplished in large-scale ill-posed inverse problems with dense system matrices, which makes it very suitable for BLT.

It is noted that the *in vivo* experiment was not as accurate as the simulations. There are many reasons responsible for this instance. In the first place, the error was generated when we mapped the energy distribution from two-dimensional images to the three-dimensional mouse surface. Second, main tissues were reserved for building a heterogeneous model, but others were simply regarded as muscle, which also led to errors. With the improvement of the experimental procedures and imaging system, reconstruction quality could be promoted. After all, it is a newly developed imaging system.

For BLT reconstruction, the DA is attractive and popular due to its moderate computational efficiency and explicit physical meaning. However, it has some limitations in certain regions, such as in the void or more absorptive regions. To solve this problem, more

complex and precise forward models have been developed. BLT reconstruction is a linear inverse problem in nature; thus the proposed method can be performed on these advanced models with fewer modifications.

In conclusion, an efficient reconstruction algorithm for BLT based on the duality and variable splitting is presented. Both simulations and the *in vivo* experiment have validated that the proposed method can accurately reconstruct the bioluminescent source without the PSR and multispectral measurements. Future work will be focused on *in vivo* experiments with probe-marked tumor models.

This paper is supported by the National Basic Research Program of China (973 Program) under Grant No. 2011CB707700; the Knowledge Innovation Project of the Chinese Academy of Sciences under Grant No. KGCX2-YW-907; the National Natural Science Foundation of China under Grant Nos. 30970780, 81000624, 81027002, 81071205, 30970778, 81071129, and 81101095; the Beijing Natural Science Foundation No. 4111004; the Science and Technology Key Project of Beijing Municipal Education Commission under Grant No. KZ200910005005; the Doctoral Fund of the Ministry of Education of China under Grant No. 20091103110005; the Fellowship for Young International Scientists of the Chinese Academy of Sciences under Grant No. 2010Y2GA03; and the Chinese Academy of Sciences Visiting Professorship for Senior International Scientists under Grant No. 2010T2G36.

References

1. V. Ntziachristos, J. Ripoll, L. V. Wang, and R. Weissleder, "Looking and listening to light: the revolution of wholebody photonic imaging," *Nat. Biotechnol.* **23**, 313–320 (2005).
2. J. K. Willmann, N. van Bruggen, L. M. Dinkelborg, and S. S. Gambhir, "Molecular imaging in drug development," *Nat. Rev. Drug Discov.* **7**, 591–607 (2008).
3. J. Tian, J. Bai, X. Yan, S. Bao, Y. Li, W. Liang, and X. Yang, "Multimodality molecular imaging," *IEEE Eng. Med. Biol. Mag.* **27**(5), 48–57 (2008).
4. A. M. Loening, A. M. Wu, and S. S. Gambhir, "Red-shifted Renilla reniformis luciferase variants for imaging in living subjects," *Nat. Med.* **4**, 641–643 (2007).
5. K. Liu, J. Tian, Y. Lu, C. Qin, X. Yang, S. Zhu, and X. Zhang, "A fast bioluminescent source localization method based on generalized graph cuts with mouse model validations," *Opt. Express* **18**, 3732–3745 (2010).
6. G. Wang, Y. Li, and M. Jiang, "Uniqueness theorems in bioluminescence tomography," *Med. Phys.* **31**, 2289–2299 (2004).
7. H. Dehghani, S. C. Davis, S. Jiang, B. W. Pogue, K. D. Paulsen, and M. S. Patterson, "Spectrally resolved bioluminescence optical tomography," *Opt. Lett.* **31**, 365–367 (2006).
8. H. Dehghani, S. C. Davis, and B. W. Pogue, "Spectrally resolved bioluminescence tomography using the reciprocity approach," *Med. Phys.* **35**, 4863–4871 (2008).
9. C. Kuo, O. Coquoz, T. L. Troy, H. Xu, and B. W. Rice, "Three-dimensional reconstruction of *in vivo* bioluminescent sources based on multispectral imaging," *J. Biomed. Opt.* **12**, 024007 (2007).
10. S. Ahn, A. J. Chaudhari, F. Darvas, C. A. Bouman, and R. M. Leahy, "Fast iterative image reconstruction methods for fully 3D multispectral bioluminescence tomography," *Phys. Med. Biol.* **53**, 3921–3942 (2008).
11. G. Wang, W. Cong, K. Durairaj, X. Qian, H. O. Shen, P. Sinn, E. Hoffman, G. McLennan, and M. Henry, "In vivo mouse

- studies with bioluminescence tomography," *Opt. Express* **14**, 7801–7809 (2006).
12. C. Qin, J. Tian, X. Yang, J. Feng, K. Liu, J. Liu, G. Yan, S. Zhu, and M. Xu, "Adaptive improved element free Galerkin method for quasi- or multi-spectral bioluminescence tomography," *Opt. Express* **17**, 21925–21934 (2009).
13. J. Feng, K. Jia, G. Yan, S. Zhu, C. Qin, Y. Lv, and J. Tian, "An optimal permissible source region strategy for multispectral bioluminescence tomography," *Opt. Express* **16**, 15640–15654 (2008).
14. K. Liu, J. Tian, X. Yang, Y. Lu, C. Qin, S. Zhu, and X. Zhang, "A fast bioluminescent source localization method based on generalized graph cuts with mouse model validations," *Opt. Express* **18**, 3732–3745 (2010).
15. Y. Lu, H. B. Machado, A. Douraghy, D. Stout, H. Herschman, and A. F. Chatziioannou, "Experimental bioluminescence tomography with fully parallel radiative-transfer-based reconstruction framework," *Opt. Express* **17**, 16681–16695 (2009).
16. Y. Lu, J. Tian, W. Cong, G. Wang, J. Luo, W. Yang, and H. Li, "A multilevel adaptive finite element algorithm for bioluminescence tomography," *Opt. Express* **14**, 8211–8223 (2006).
17. Y. Lu, X. Zhang, A. Douraghy, D. Stout, J. Tian, T. F. Chan, and A. F. Chatziioannou, "Source reconstruction for spectrally-resolved bioluminescence tomography with sparse a priori information," *Opt. Express* **17**, 8062–8080 (2009).
18. X. He, J. Liang, X. Qu, H. Huang, Y. Hou, and J. Tian, "Truncated total least squares method with a practical truncation parameter choice scheme for bioluminescence tomography inverse problem," *Int. J. Biomed. Imaging* **2010**, 291874 (2010).
19. H. Gao and H. Zhao, "Multilevel bioluminescence tomography based on radiative transfer equation. Part 1: L1 regularization," *Opt. Express* **18**, 1854–1871 (2010).
20. X. He, J. Liang, X. Wang, J. Yu, X. Qu, X. Wang, Y. Hou, D. Chen, F. Liu, and J. Tian, "Sparse reconstruction for quantitative bioluminescence tomography based on the incomplete variables truncated conjugate gradient method," *Opt. Express* **18**, 24825–24841 (2010).
21. J. M. Bioucas-Dias and M. A. T. Figueiredo, "Multiplicative noise removal using variable splitting and constrained optimization," *IEEE Trans. Image Process.* **19**, 1720–1730 (2010).
22. D. Han, J. Tian, S. Zhu, J. Feng, C. Qin, B. Zhang, and X. Yang, "A fast reconstruction algorithm for fluorescence molecular tomography with sparsity regularization," *Opt. Express* **18**, 8630–8646 (2010).
23. D. Han, J. Tian, C. Qin, B. Zhang, K. Liu, and X. Ma, "A fast reconstruction method for fluorescence molecular tomography based on improved iterated shrinkage," *Proc. SPIE* **7965**, 79651C (2011).
24. C. Wu and X. Tai, "Augmented lagrangian method, dual methods, and split Bregman iteration for ROF, vectorial TV, and high order models," *SIAM J. Imaging Sci.* **3**, 300–339 (2010).
25. S. Setzer, "Operator splittings, Bregman methods and frame shrinkage in image processing," *Int. J. Comput. Vis.* **92**, 265–280 (2011).
26. M. Schweiger, S. R. Arridge, M. Hiraoka, and D. T. Delpy, "The finite element method for the propagation of light in scattering media: boundary and source conditions," *Med. Phys.* **22**, 1779–1792 (1995).
27. A. D. Klose, V. Ntziachristos, and A. H. Hielscher, "The inverse source problem based on the radiative transfer equation in optical molecular imaging," *J. Comput. Phys.* **202**, 323–345 (2005).
28. H. Gao, H. Zhao, W. Cong, and G. Wang, "Bioluminescence tomography with Gaussian prior," *Biomed. Opt. Express* **1**, 1259–1277 (2010).
29. A. Cong, W. Cong, Y. Lu, P. Santago, A. Chatziioannou, and G. Wang, "Differential evolution approach for regularized bioluminescence tomography," *IEEE Trans. Biomed. Eng.* **57**, 2229–2238 (2010).
30. R. Tomioka and M. Sugiyama, "Dual augmented Lagrangian method for efficient sparse reconstruction," *IEEE Signal Process. Lett.* **16**, 1067–1070 (2009).
31. M. Freiburger, C. Clason, and H. Scharfetter, "Total variation regularization for nonlinear fluorescence tomography with an augmented Lagrangian splitting approach," *Appl. Opt.* **49**, 3741–3747 (2010).
32. S. Kim, K. Koh, M. Lustig, S. Boyd, and D. Gorinevsky, "An interior-point method for large-scale L1-regularized least squares," *IEEE J. Sel. Top. Signal Process.* **1**, 606–617 (2007).
33. J. Feng, K. Jia, C. Qin, G. Yan, S. Zhu, X. Zhang, J. Liu, and J. Tian, "Three-dimensional bioluminescence tomography based on Bayesian approach," *Opt. Express* **17**, 16834–16848 (2009).
34. Y. Lu, J. Tian, W. Cong, G. Wang, W. Yang, C. Qin, and M. Xu, "Spectrally resolved bioluminescence tomography with adaptive finite element analysis: methodology and simulation," *Phys. Med. Biol.* **52**, 4497–4512 (2007).
35. X. Ma, J. Tian, X. Yang, C. Qin, S. Zhu, and Z. Xue, "Research on liver tumor proliferation and angiogenesis based on multimodality molecular imaging," *Acta Biophys. Sin.* **27**, 355–364 (2011).
36. X. Ma, J. Tian, C. Qin, X. Yang, B. Zhang, Z. Xue, X. Zhang, D. Han, D. Dong, and X. Liu, "Early detection of liver cancer based on bioluminescence tomography," *Appl. Opt.* **50**, 1389–1395 (2011).
37. B. Zhang, X. Yang, C. Qin, D. Liu, S. Zhu, J. Feng, L. Sun, K. Liu, D. Han, X. Ma, X. Zhang, J. Zhong, X. Li, X. Yang, and J. Tian, "A trust region method in adaptive finite element framework for bioluminescence tomography," *Opt. Express* **18**, 6477–6491 (2010).
38. G. Alexandrakis, F. R. Rannou, and A. F. Chatziioannou, "Tomographic bioluminescence imaging by use of a combined optical-PET (OPET) system: a computer simulation feasibility study," *Phys. Med. Biol.* **50**, 4225–4241 (2005).